Radio Science

RESEARCH ARTICLE
10.1029/2025RS008543

Six-Component Electromagnetic Wave Measurements of Sprite-Associated Lightning

Martin Füllekrug[1], Michael Kosch[2,3], Gavin Dingley[1], Xue Bai[1], and Liliana Macotela[1,4]

[1]Department of Electronic and Electrical Engineering, University of Bath, Bath, UK, [2]South African National Space Agency, Hermanus, South Africa, [3]Department of Physics, Lancaster University, Lancaster, UK, [4]Earth Observation Group, Norwegian Research Centre, Tromso, Norway

Key Points:

- Six electromagnetic field components of sprite-producing lightning are measured simultaneously
- The coupling between electric fields and magnetic fields enables the calculation of magnetic fields from measured electric fields
- The peak energy flux of sprite-associated lightning varies between ∼10–1,000 μW/m^2 at distances ∼400–430 km

Correspondence to:
M. Füllekrug,
eesmf@bath.ac.uk

Citation:
Füllekrug, M., Kosch, M., Dingley, G., Bai, X., & Macotela, L. (2026). Six-component electromagnetic wave measurements of sprite-associated lightning. *Radio Science*, *61*, e2025RS008543. https://doi.org/10.1029/2025RS008543

Received 7 NOV 2025
Accepted 21 JAN 2026

Author Contributions:
Conceptualization: Martin Füllekrug, Michael Kosch
Data curation: Martin Füllekrug
Formal analysis: Martin Füllekrug
Funding acquisition: Michael Kosch
Investigation: Martin Füllekrug, Gavin Dingley, Xue Bai, Liliana Macotela
Methodology: Martin Füllekrug, Michael Kosch
Project administration: Martin Füllekrug
Resources: Martin Füllekrug, Michael Kosch
Software: Martin Füllekrug
Validation: Martin Füllekrug, Michael Kosch
Visualization: Martin Füllekrug
Writing – original draft: Martin Füllekrug
Writing – review & editing: Martin Füllekrug, Michael Kosch, Gavin Dingley, Xue Bai, Liliana Macotela

Abstract Low frequency electromagnetic waves emitted by sprite-producing lightning are normally measured using vertical electric fields or horizontal magnetic fields. Here we report for the first time the simultaneous measurement of electromagnetic waves from sprite-producing lightning in all six electromagnetic field components E_x, E_y, E_z, H_x, H_y, and H_z. A rigorous assessment of the horizontal electric field measurements with dipole antennas in two independent calibration experiments shows that a timing uncertainty of $\sim 1-2$ ns can be achieved, well above the current fundamental limit of the timing accuracy ∼1–5 ps. The coupling between the electric and magnetic fields is quantified using a transfer matrix, allowing the magnetic field to be reconstructed accurately from electric field measurements. The cross product of electric and magnetic fields is used to calculate peak energy fluxes and arrival azimuths from sprite-producing lightning. It is found that peak energy fluxes vary between ∼10–1,000 μW/m^2 and that the differences between the measured and expected arrival azimuths are practically normally distributed with a mean and standard deviation of $-8.0° \pm 2.2°$. It is concluded that horizontal electric field measurements are well suited to characterize electromagnetic waves with added benefits, including the ease of deployment in harsh environments, cost-effectiveness and scalability, for example for polarisation measurements in large low frequency arrays. The significance of this study is that it can be used as a pathfinder mission to identify critical technical requirements for the array deployment during the Africa2Moon lander mission.

Plain Language Summary Sprites are Transient Luminous Events above thunderclouds that tend to occur after intense lightning activity. The lightning emits electromagnetic waves that can be recorded hundreds of kilometres away. The electromagnetic waves are composed out of six different components. Here we report for the first time the simultaneous measurement of all six components. It is found that all the six components are well related to each other with very high precision. For the deployment of arrays with a large number of measurement instruments, it is therefore possible to choose horizontal electric field measurements which are cost-effective and logistically convenient, in particular in harsh environments. At the same time, such array experiments can be used as a pathfinder mission for the planned deployment of an astronomical array on the far side of the moon to detect celestial objects which cannot be measured at the surface of the Earth.

1. Introduction

Sprites are Transient Luminous Events (TLEs) that tend to occur above thunderclouds when a spatially extended charge distribution inside the thundercloud is neutralized (e.g., Füllekrug et al., 2006; Pasko, 2010; Zhang et al., 2024, and references therein), for example, by intense positive lightning discharges and/or large scale in-cloud lightning activity, commonly known as "spider lightning" (e.g., Haspel & Yair, 2024; Lyons, 1996, and references therein). The electromagnetic fields radiated by sprite-producing lightning discharges are mainly measured with horizontal magnetic fields or with vertical electric fields (e.g., Bai & Füllekrug, 2022; Bor et al., 2018; Cummer & Inan, 1997; Füllekrug et al., 2001; Pizzuti et al., 2022; Reising et al., 1999, 1996, and references therein). Horizontal magnetic fields are either measured with air-core loop antennas (e.g., Fraser-Smith, 2007; Fraser-Smith et al., 1991, and references therein) or with induction coils (e.g., Bor et al., 2018, 2016; Whitley et al., 2011, and references therein], whereas vertical electric fields are measured with monopole or dipole antennas (e.g., Füllekrug, 2010, and references therein). Lightning interferometry that measures the arrival azimuth and elevation angles of electromagnetic waves emitted by atmospheric discharge processes, such as streamers, leaders, return strokes and continuing current, require a large number of receivers where the logistic effort and cost implications become significant such that the measurement of vertical electric fields at low

frequencies ∼0.1–500 kHz is commonly preferred (e.g., Bitzer et al., 2013; Füllekrug, Mezentsev, et al., 2015; Füllekrug, Smith, et al., 2015; Füllekrug et al., 2014, 2016, 2018a, 2018b; Karunarathne et al., 2013; Lyu et al., 2016; Mezentsev & Füllekrug, 2013; Qu et al., 2018; Shi et al., 2017; Smith et al., 2002; Wu et al., 2018; Yoshida et al., 2016; Zhu et al., 2021, and references therein).

The electromagnetic boundary conditions at the surface of a perfect horizontal conductor, which has no electromagnetic fields inside, are that the vertical electric field and the horizontal magnetic fields can jump from a finite value at the surface to zero inside, whereas the horizontal electric field and vertical magnetic field have to be continuous and are hence zero at the surface of the perfect conductor (Jackson, 1999). The Earth's uppermost layers have a finite conductivity such that the primary electromagnetic fields from lightning discharges induce surface currents with secondary electromagnetic fields that can be observed at the surface of the Earth (Bor et al., 2022; Wait, 1990), even though they are much smaller, that is, on the order of a few tens of percent when compared to the primary fields. As a result, measurements of vertical electric fields or horizontal magnetic fields are commonly preferred. At frequencies <0.1 kHz, vertical electric fields and horizontal magnetic fields are measured sometimes together (e.g., Burke & Jones, 1992, 1995; Nakamura et al., 2010, and references therein) to calculate the distances between lightning discharges and the receiver using the electromagnetic wave impedance, or to approximate measurements of the complete Poynting vector. However, the frequency bandwidth of a magnetic field sensor is limited as a result of the coil's resonance and the technology does not easily scale up to low-frequency interferometry with numerous sensors in large arrays. As a result, the measurement of horizontal electric fields with dipole antennas might be advantageous, in particular for deployments in harsh environments. For example, the vertical stability of antennas would need to withstand the fierce winds in the Antarctic and avoid the static arising from charged ice crystals.

This contribution aims to explore the use of horizontal electric field measurements along with exemplary measurements of all six electromagnetic field components of sprite-producing lightning discharges during field work in the Karoo desert in South Africa on 26 January 2023. The contribution describes the instruments used with particular emphasis on tests in the laboratory and in the field to quantify the timing uncertainties that are relevant for interferometric experiments. Subsequently, simultaneous measurements of all six electromagnetic field components E_x, E_y, E_z, H_x, H_y, and H_z are conducted and evaluated in two ways: first by comparing the electric field measurements to the magnetic field measurements using a transfer matrix, and second by using the cross product between the electric and magnetic field vectors to calculate peak energy fluxes and arrival azimuths of electromagnetic waves from sprite-producing lightning discharges. The main advantage of measuring all six electromagnetic field components simultaneously is that it is possible to assess whether the horizontal electric field components are consistent with the other four electromagnetic field directions. If this is so, the number of horizontal electric field sensors can be scaled up to very large arrays for use in low-frequency interferometry.

2. Instrument

The instrument for the simultaneous measurement of six electromagnetic field components extends a previous instrument to measure vertical electric fields (Füllekrug, 2010). The novel instrument is composed of six electromagnetic field sensors and a timed data acquisition disciplined by a Global Navigation Satellite System (GNSS) clock.

2.1. Signal Conditioning

The wavelengths of the incident electromagnetic waves at low frequencies are much larger than the length of electric and magnetic field sensors, e.g., ∼1 km at 300 kHz and ∼10 km at 30 kHz. This means that the measurements of voltages are in essence of a quasi-static, or capacitive, nature. As a result, a high impedance follower, or impedance converter, is required to match the output impedance of electric field sensors to the input impedance of the data acquisition. The impedance converter is combined here with a bandpass filter to form an analogue signal conditioning unit. The electronic circuit diagram of the analogue signal conditioning unit is shown in Figure 1a. The signal from the electric field sensor is initially amplified by a high impedance Junction Field Effect Transistor (JFET) powered by 12 V DC provided by a battery. The finite capacitance and resistance of the JFET act simultaneously as a high pass filter for the incoming signal. The second part of the signal conditioning unit consists of a three-stage inductance/capacitance (LC) low-pass filter, where the capacitance values vary between

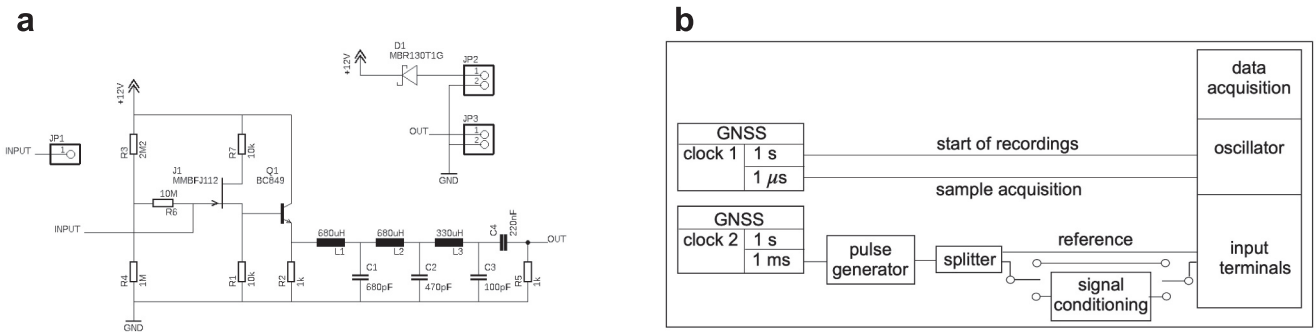

Figure 1. Analogue signal conditioning and test setup. (a) The analogue signal from an electric field sensor is amplified by a high impedance Junction Field Effect Transistor (JFET) powered by 12 V DC. The analogue signal conditioning unit thereby acts as a high impedance follower, or impedance converter. The finite capacitance and resistance of the JFET effectively acts as a high-pass filter. Subsequently, the signal is conditioned with a passive three stage inductance/capacitance (LC) low-pass filter. (b) The block diagram shows the test setup for the signal conditioning unit. One Global Navigation Satellite System (GNSS) clock generates every 1 s a rectangular pulse to start the recordings of the data acquisition, along with a time aligned pulse every 1 μs that triggers the acquisition of each individual sample. The second GNSS clock acts as a signal generator that produces rectangular pulses every 1 ms where the rising edge is converted by the pulse generator to a 1 μs long Kronecker delta pulse. The splitter divides the signal into a reference signal and a signal that is either fed directly to the input terminals, or through the signal conditioning unit for comparison with the reference signal.

stages to minimize the risk of hardware saturation, since capacitors can become fully charged, or saturated, by nearby lightning discharges.

2.2. Data Acquisition and Timing

The data acquisition NI-USB 6366 from National Instruments offers the parallel measurement of up to eight channels. Here, six channels are used to simultaneously measure the six electromagnetic field components with a sampling frequency of 1 MHz. The onboard oscillator is synchronised to Coordinated Universal Time (UTC) by a commercial GNSS clock, the u-blox EVK-F9T. The first timing signal is the Pulse Per Second (PPS) where the rising edge of a rectangular, or Transistor-Transistor Logic (TTL), pulse marks the start time of the UTC second. The second timing signal of the GNSS clock is a 1 μs long TTL pulse with a 50% duty cycle to trigger the acquisition of each individual sample by disciplining the onboard sample clock. This strategy results in a timed data acquisition with a sampling frequency of 1 MHz which is as precise as possible. In this way, the overall timing uncertainty is mainly determined by the accuracy of the GNSS clock which is quantified in detail in the following section.

2.3. Timing Uncertainty

The timing uncertainty of electromagnetic measurements is the most important factor that determines the performance and design of low frequency arrays. GNSS clocks are nowadays commonly used to discipline the local oscillator that controls the data acquisition with the aim to minimize long-term drift, or wander, in the recordings. The timing uncertainties on relatively short time scales, known as jitter, are commonly attributed to stray, or parasitic, capacitances in electronic systems. The time it takes to charge and discharge a capacitance is influenced by small fluctuations in the capacitance arising from electronic noise. This effect can result in small advances and/or delays of the zero crossings, or polarity transitions, of the timing signals used for synchronisation. It is practically impossible to avoid stray capacitances when manufacturing electronic circuit boards. It is therefore of fundamental importance to characterize timing uncertainties to quantify limitations for the subsequent interpretation of results.

In this contribution, the timing uncertainties caused by the analogue signal conditioning unit are quantified by comparison of a reference signal with a signal that is fed through the analogue signal conditioning unit or bypasses it. These two experiments are explained in the following, assisted by the block diagram shown in Figure 1b.

The key elements of the data acquisition are the onboard oscillator and the input terminals (compare to Section 2.2). An independent GNSS clock acts as a signal generator that produces rectangular pulses every 1 ms with a 50% duty cycle, where the rising edge is converted to a 1 μs long Kronecker delta pulse, that is, one single sample, by the pulse generator Hewlett Packard (8082A). A signal splitter from Mini-Circuits (ZFRSC-42-S+)

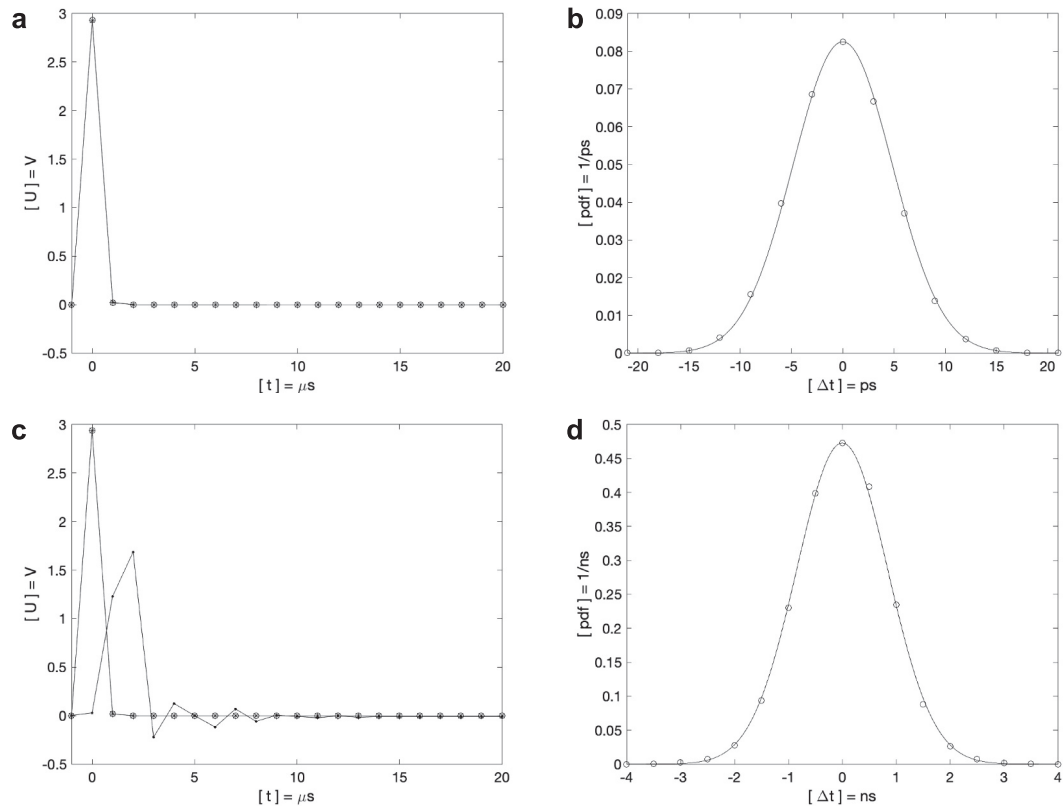

Figure 2. Test results of the analogue signal conditioning. (a) The splitter and parallel data acquisition are tested by bypassing the signal conditioning unit. The reference signal (circles) is practically identical to the signal that bypasses the signal conditioning unit and the reconstructed reference signal (stars) by calculating and applying the inverse impulse response function. (b) The probability density function (pdf) of the time differences between the reference signal and the reconstructed reference signal (circles) are practically normally distributed (solid line) with a mean and standard deviation of 0.0 ± 4.8 ps. (c) The reference is signal is a Kronecker delta pulse (circles) which is compared to the impulse response of the analogue signal conditioning unit (dots) that is used to reconstruct the reference signal (stars) by calculating and applying the inverse impulse response function. (d) The pdf of the time differences between the reference signal and the reconstructed reference signal (circles) is practically normally distributed (solid line) with a mean and standard deviation of 0.0 ± 0.8 ns. The uncertainty ∼0.8 ns is attributed to stray capacitances in the signal conditioning unit.

divides the signal into a reference signal and a signal that goes through a switch which either feeds the signal directly to the input terminals of the data acquisition, or through the signal conditioning unit for comparison with the reference signal. The main advantage of this arrangement is that a fundamental limit of the timing uncertainty can be determined by bypassing the signal conditioning unit for comparison with the reference signal. In this case, it is possible to test how much timing uncertainty is contributed by the splitter, the Bayonet Neill-Concelman (BNC) cables and connectors, the parallel boards of the data acquisition, and the software to calculate the timing uncertainty. In this contribution, the timing uncertainty is calculated from the harmonically interpolated cross-covariance function in the time domain which is commonly used to determine time differences digitally with a precision that is smaller than the sampling time interval (Füllekrug et al., 2001; Stock et al., 2014).

This rigorous test protocol shows that the fundamental limit of the timing uncertainty is -40.0 ± 4.8 ps when the reference signal is compared to the signal that bypasses the signal conditioning unit. The uncertainty of 4.8 ps is much smaller than the offset of −40 ps. It is therefore concluded that the offset is either introduced by the splitter, or by the sampling delay of the parallel channels of the data acquisition, but not by the software that is used to calculate the time differences. It is advantageous to treat the signal that bypasses the signal conditioning unit as the impulse response of the reference signal. In this case, it is possible to reconstruct the reference signal by calculating and applying the inverse impulse response to the signal that bypasses the signal conditioning unit (Figure 2a). This is effectively the same methodology that will be applied to the impulse response of the signal

conditioning unit. In this way, the offset of −40.0 ps is removed and only the jitter of 4.8 ps remains to describe the fundamental limit of the timing uncertainty (Figure 2b).

The same methodology is applied to the signal that is fed through the signal conditioning unit to measure its impulse response and to calculate the time differences between the reference signal and the reconstructed reference signal (Figure 2c). The timing uncertainty introduced by the signal conditioning unit is 0.0 ± 0.8 ns, that is, well above the fundamental uncertainty limit of 4.8 ps. The timing uncertainty is similar to the uncertainty for two independently operating GNSS clocks such that there is no uncertainty added by the signal conditioning unit, even though the fundamental timing uncertainty limit is much smaller. This increase of the timing uncertainty is attributed to the stray capacitance arising from the proximity of conductors and electronic components on the printed circuit board of the signal conditioning unit which act like unintentional, yet finite, capacitances. This interpretation is corroborated by numerical simulations of the phase of the impulse response of the signal conditioning unit which agrees well with the measured phase response. Given that the capacitance plays such a significant role, a calibration during experiments in the field with simultaneous recordings of multiple horizontal electric field antennas appears to be sensible, as described in the following two sections.

2.4. Electric and Magnetic Field Sensors

Two types of electric field sensors are used here to measure the three electric field components, that is, one vertical electric field antenna and two orthogonal horizontal electric field antennas. The vertical electric field antenna is a 1 cm thick circular flat plate with a 1 m^2 surface area that is elevated 1.5 m above the ground by three nylon 66 rods to insulate the plate from the ground (Füllekrug, 2010). The horizontal electric fields are measured with shielded twisted pair cables with two core wires. The shield attracts the electric field lines into the two core wires, where each twist of the two wires increases the capacitance of the cable. Two cables are aligned in opposite directions and the voltage difference between two core wires in the cables is measured at the center. Each of the two cables is 6 m long, where one core is used to measure the signal voltage, such that the electric field is calculated from the measured voltage difference between the two cables divided by $2 \cdot 6$ m = 12 m to obtain the electric field. This arrangement effectively corresponds to a dipole antenna to measure horizontal electric fields.

The three magnetic field components are measured with commercial induction coils, that is Metronix MFS-07, which measure the magnetic field in the frequency range from ∼4 Hz to ∼50 kHz (Whitley et al., 2011).

3. Horizontal Electric Field Measurements

Two different measurements of horizontal electric fields with dipole antennas are conducted to determine the timing uncertainties in real world situations. Both experiments are carried out in the proximity of the Square Kilometer Array (SKA) on private farmland near the town of Carnarvon in the Karoo desert, South Africa (lat: −30.955°, lng: 22.105°), from 25–26 January 2023. The first experiment simultaneously measures the electric fields with six horizontal dipole antennas aligned in parallel next to each other to cross calibrate the signals. The second experiment uses six dipole antennas rotated relative to each other. This geometric arrangement is intended to investigate whether the orientation of the dipole antenna has a significant effect on the timing uncertainty.

In the first experiment, six dipole antennas are aligned in parallel. The signals from five dipole antennas are cross calibrated with transfer functions to one dipole antenna. The signal conditioning unit of this dipole antenna has been used for vertical electric field measurements of the timing transmitter operating at 60 kHz in Cumbria, UK, which is intended for an approximate calibration of electric field measurements (Füllekrug et al., 2018b, Section 3.2). The cross-calibrated horizontal electric fields from distant lightning events agree well (Figure 3a). A total of 870 lightning strokes are extracted from the parallel recordings. The timing differences between all $15 = 6!/(2!(6-2)!)$ possible pairs of the six dipole antennas results in $13050 = 15 \cdot 870$ timing differences which are summarized in one probability density function (pdf). This pdf is a double exponential, or Laplacian, distribution function (Figure 3b) described by

$$f(x) = \frac{1}{2b}\exp\left(\frac{-|x-\mu|}{b}\right) \quad [1/\text{ns}], \tag{1}$$

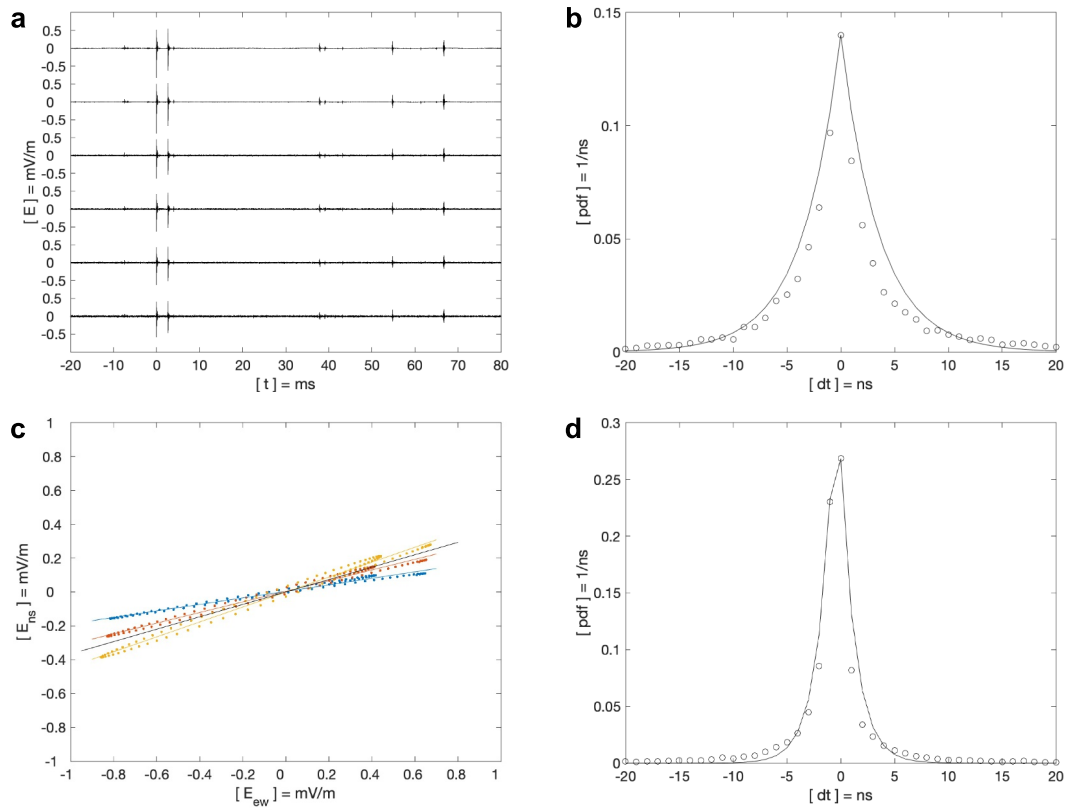

Figure 3. Horizontal electric field measurements. (a) Parallel horizontal field recordings with 12 m long dipole antennas are used to cross-calibrate six different signal conditioning units. The recordings show two large lightning strokes followed by smaller strokes tens of ms later. (b) The pdf of the time differences of selected strokes (circles) is practically a double exponential distribution (solid line) with a mean and standard deviation of 0.0 ± 5.0 ns. (c) Three orthogonal horizontal electric field measurements with dipole antennas oriented 0°, 30°, and 60° from geographic north are rotated onto east-west (ew) and north-south (ns) cartesian coordinates (blue, red and yellow lines and dots). The arrival direction of the electromagnetic waves is compared to the expected arrival azimuth from a sprite-producing lightning stroke (black line). The horizontal electric fields are aligned with the surface current in the conductive Earth. (d) The pdf of the time differences between the rotated horizontal electric fields of lightning strokes ("circles") is practically a double exponential (solid line) with a mean and standard deviation of −0.4 ± 2.0 ns.

where x is the variate, μ is the mean of the double exponential pdf and b is a scaling parameter. The standard deviation of the pdf can be calculated from the scaling parameter $\sigma = \sqrt{2}b$ such that the timing uncertainty is 0.0 ± 5.0 ns, which is similar to the timing uncertainty measured in the laboratory. The pdf of time differences measured in the laboratory is a normal distribution (Figure 2d) while the parallel calibration is best described with a double exponential distribution (Figure 3b). This difference is attributed to the different measurement of the time differences. For the Kronecker delta pulses of the reference signal and the reconstructed reference signal in the laboratory, 4 samples are used to calculate the time differences, whereas the time differences of real world signals are calculated from the envelope of the complex trace with 200 samples which results in a robust estimate of the time differences of real world signals.

In the second experiment, six dipole antennas are rotated in angular steps of 30° with respect to each other, that is, at 0°, 30°, 60°, 90°, 120°, and 150°, where 0° corresponds to the geographic north direction and the rotation angles are counted clockwise. This arrangement can be understood to form three cartesian measurement systems or one single measurement system where the outer end points of the cables form a dodecagon with 12 vertices. This geometric structure is reminiscent of spider webs which resulted in the more colloquial designation "spider antenna." Similar antennas are used for infrasound measurements to enhance the signal-to-noise ratio of the original recordings (e.g., Alcoverro & LePichon, 2005, and references therein). The horizontal electric field

recordings in the three different cartesian coordinate systems are rotated into the geographic north/south and east/west directions for comparison

$$\begin{pmatrix} E_x \\ E_y \end{pmatrix} = \begin{pmatrix} \cos\varphi & \sin\varphi \\ -\sin\varphi & \cos\varphi \end{pmatrix} \begin{pmatrix} E_{x_o} \\ E_{y_o} \end{pmatrix} \quad [\mathrm{V/m}], \tag{2}$$

where E_x is aligned in the geographic east/west direction, E_y in the north/south direction, φ is the rotation angle to revolve the coordinate system clockwise by 0°, 30°, and 60°, and E_{x_o} and E_{y_o} are the measurements in the original cartesian coordinates. In this way, it is possible to compare the polarisation of horizontal electric fields, for example, from one sprite-producing lightning stroke (Figure 3c). The rotated horizontal electric fields, originally measured in three different coordinate systems, are predominantly linearly polarized. The major axes of the narrow polarisation ellipses are aligned within a few degrees of the expected arrival azimuth that is calculated from the location of the lightning stroke reported by Earth Networks Total Lightning Network (ENTLN). The polarisation axis is aligned with the induced surface current caused by the skin-effect such that the incident horizontal electric field perpendicular to the direction of travel in vacuum appears to be rotated by 90°. The inferred arrival azimuths exhibit an uncertainty of $\sim\pm 6°$ which is attributed to conductivity inhomogeneities inside the Earth (Wait, 1990) which can channel the surface current into a preferential direction. Given this relatively large uncertainty, horizontal electric fields cannot be used for direction finding, similar to horizontal magnetic fields, both of which have been abandoned for use in lightning location in favor of arrival time difference analyses. A more rigorous analysis extracts 5705 lightning strokes from the recordings for a statistical analysis of the timing uncertainties. In this case, the horizontal electric fields of each individual stroke are rotated into geographic coordinates, the complex trace is calculated for the north/south and east/west directions and the envelope *Ea* of these two component measurements is calculated from

$$E_a = \sqrt{\begin{pmatrix} E_x \\ E_y \end{pmatrix}^T \cdot \begin{pmatrix} E_x \\ E_y \end{pmatrix}} = \left\| \begin{pmatrix} E_x \\ E_y \end{pmatrix} \right\| \quad [\mathrm{V/m}], \tag{3}$$

where the multiplication with the conjugate vector transposition ^{T} results in a real valued vector norm on the right hand side. The time differences between all 3 possible pairs of envelopes of the three cartesian coordinate systems results $17115 = 3 \cdot 5705$ time differences which are summarized in one pdf (Figure 3d). The pdf is a double exponential with a timing uncertainty -0.4 ± 2.0 ns. This timing uncertainty is smaller than the timing uncertainty of the six individual electric field measurements (Figure 3b). This small reduction of the standard deviation is attributed to the two component electric field measurements which are combined by the vector norm to calculate one time difference.

In summary, both measurements of naturally occurring horizontal electric fields with dipole antennas which are either aligned in parallel, or rotated with respect to each other, exhibit timing uncertainties ~2–5 ns. These observed timing uncertainties are consistent with the timing uncertainties of the signal conditioning unit measured in the laboratory and they are in line with the accuracy of the GNSS clocks used. It is therefore concluded that horizontal electric field measurements offer an attractive novel alternative to measure time differences of electromagnetic fields from lightning strokes. In particular, this enables simultaneous measurements of all six electromagnetic field components of sprite-producing lightning as described in the following section.

4. Electric and Magnetic Field Measurements

The first simultaneous measurements of six electromagnetic field components E_x, E_y, E_z, H_x, H_y, and H_z from a sprite-producing lightning stroke are shown in Figure 4. The positive lightning stroke at 0 ms is followed by a ~100 ms long enhancement of the horizontal electric and magnetic field components, which are attributed to consecutive in-cloud lightning leaders (e.g., Johnson & Inan, 2000; Lapierre et al., 2017; Marshall et al., 2007; Ohkubo et al., 2005, and references therein). The polarity of the vertical electric field is negative, which corresponds to a positive lightning discharge in line with atmospheric electric field convention. The induction coils originally measure the magnetic flux densities B which are converted to magnetic field strengths H by division with the magnetic field constant μ_0. The electric and magnetic fields are both bandpass filtered in the frequency

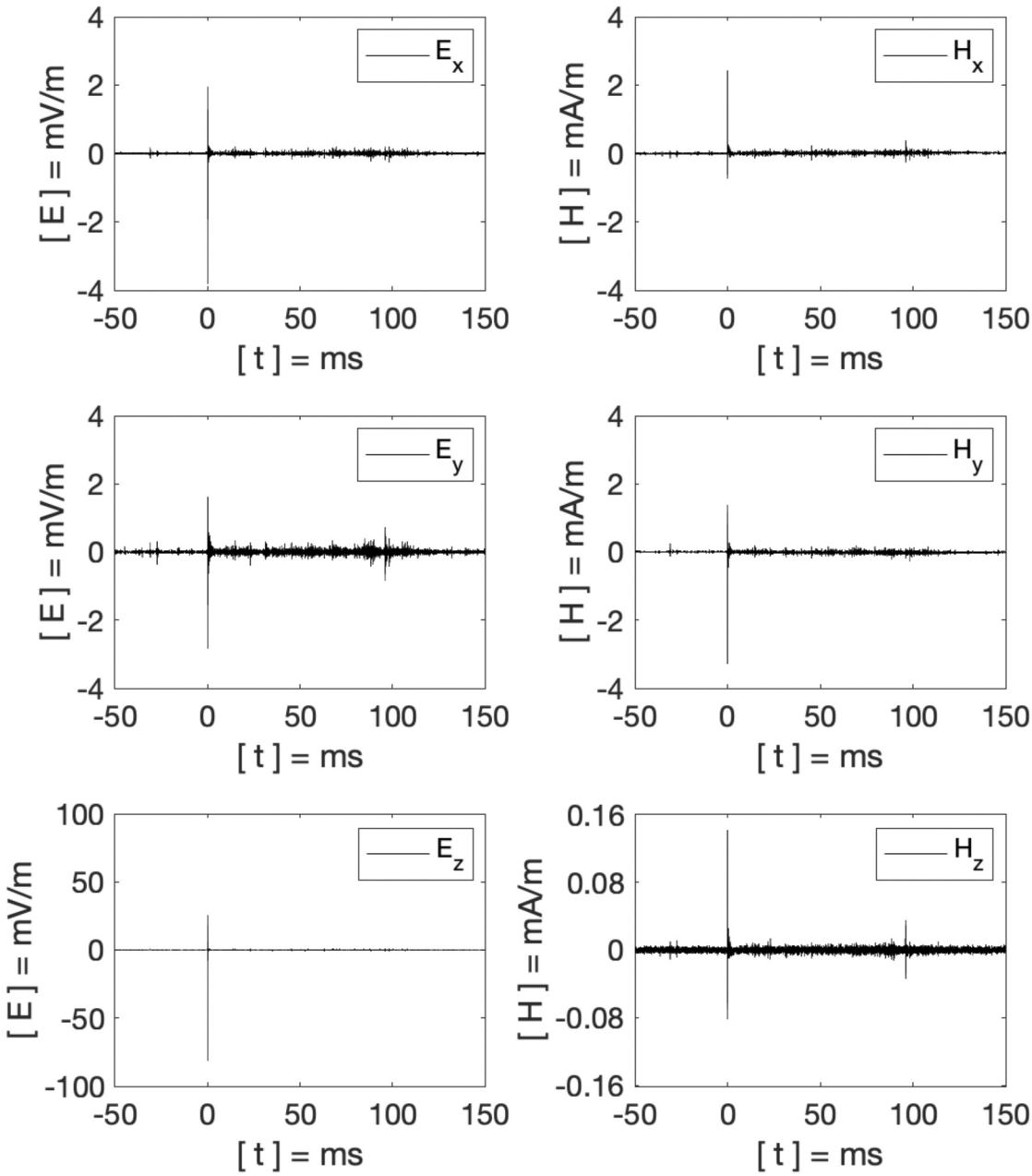

Figure 4. Electric and magnetic field measurements of all six electromagnetic field components E_x, E_y, E_z, H_x, H_y, and H_z. The large signal at 0 ms is from a sprite-producing lightning. The subsequent enhancement for 100 ms is attributed to consecutive in-cloud lightning strokes.

range from 200 Hz to 50 kHz. The high pass filter is to reduce the impact of power line harmonic radiation and the low pass filter is to match the upper limit of the magnetic field sensors. The horizontal electric fields and the vertical magnetic field are about one order of magnitude smaller than the vertical electric field and the horizontal magnetic fields. It is interesting to note that the signal-to-noise ratio of the vertical electric field of the positive lightning stroke appears to be largest which is attributed to the relatively small contribution of the consecutive in-cloud lightning leaders dominated by more horizontal current flow. The polarisation of the measurements is most apparent from a stroke that occurs at ∼90 ms in the electric north/south component E_y which is paralleled by a similar stroke in the magnetic east/west component H_x. The inhomogeneous conductivity inside the Earth results in a corresponding signal in the magnetic vertical component H_z. In summary, the measured electric and magnetic

field components are broadly consistent and coupled with each other. This coupling is quantified in more detail with a transfer matrix as described in the following section.

4.1. Coupling of Electric and Magnetic Fields

Two different types of electromagnetic coupling are investigated. The first method relates the measured electric fields with a transfer matrix to the measured magnetic fields. The second method uses the vector product of the electric and magnetic fields to calculate the energy flux perpendicular to the electric and magnetic fields, similar to the Poynting vector.

The first method operates in the spectral domain to calculate a frequency dependent transfer matrix $\underline{\underline{Z}}$ that describes the coupling of the electric field vector $\underline{E}$ with the magnetic field vector $\underline{H}$. This transfer matrix describes the effectiveness of lightning current to produce coupled electric and magnetic fields measured at remote distances on the surface of the Earth. The transfer matrix has the physical unit of conductivity which is measured in Siemens. The transfer matrix is reminiscent of the admittance that is used in electronic circuits to characterize the ease of current flow. At each frequency, the complex spectral coefficients of the electric and magnetic field vectors are coupled to each other by

$$\underline{H} = \underline{\underline{Z}}^T \underline{E} \quad [\mathrm{A/m}], \tag{4}$$

where the transfer matrix $\underline{\underline{Z}}$ is unknown and remains to be determined. This equation can be solved by applying the complex transpose on both sides

$$\underline{E}^T \underline{\underline{Z}} = \underline{H}^T \quad [\mathrm{A/m}] \tag{5}$$

to produce an overdetermined complex linear system of equations when multiple realizations of the same spectral coefficients are used. It is illuminating to formulate Equation 5 more specifically in cartesian coordinates for n realizations that are enumerated with indices varying from $1,\ 2,\ \ldots n$ such that

$$\underbrace{\begin{pmatrix} {E_{x_1}}^* & {E_{y_1}}^* & {E_{z_1}}^* \\ {E_{x_2}}^* & {E_{y_2}}^* & {E_{z_2}}^* \\ \vdots & \vdots & \vdots \\ {E_{x_n}}^* & {E_{y_n}}^* & {E_{z_n}}^* \end{pmatrix}}_{\underline{\underline{E}}^T} \begin{pmatrix} Z_{xx} & Z_{xy} & Z_{xz} \\ Z_{yx} & Z_{yy} & Z_{yz} \\ Z_{zx} & Z_{zy} & Z_{zz} \end{pmatrix} = \underbrace{\begin{pmatrix} {H_{x_1}}^* & {H_{y_1}}^* & {H_{z_1}}^* \\ {H_{x_2}}^* & {H_{y_2}}^* & {H_{z_2}}^* \\ \vdots & \vdots & \vdots \\ {H_{x_n}}^* & {H_{y_n}}^* & {H_{z_n}}^* \end{pmatrix}}_{\underline{\underline{H}}^T} \quad [\mathrm{A/m}], \tag{6}$$

where * denotes complex conjugation and each indexed row of the matrices $\underline{\underline{E}}^T$ and $\underline{\underline{H}}^T$ represents one realisation of spectral coefficients at a given frequency in cartesian coordinates. This overdetermined complex linear system of equations can be solved with the complex Gaussian minimization of least squares. In this case, Equation 6 is multiplied with the matrix $\underline{E}$ on both sides

$$\underline{\underline{E}}\ \underline{\underline{E}}^T \underline{\underline{Z}} = \underline{\underline{E}}\ \underline{\underline{H}}^T \quad [\mathrm{W/m^2}], \tag{7}$$

where $\underline{\underline{E}}\ \underline{\underline{E}}^T$ and $\underline{\underline{E}}\ \underline{\underline{H}}^T$ are 3×3 matrices. Multiplication with the inverse matrix $\left(\underline{\underline{E}}\ \underline{\underline{E}}^T\right)^{-1}$ on both sides then results in the transfer matrix

$$\underline{\underline{Z}} = \left(\underline{\underline{E}}\ \underline{\underline{E}}^T\right)^{-1} \underline{\underline{E}}\ \underline{\underline{H}}^T \quad [\mathrm{S}], \tag{8}$$

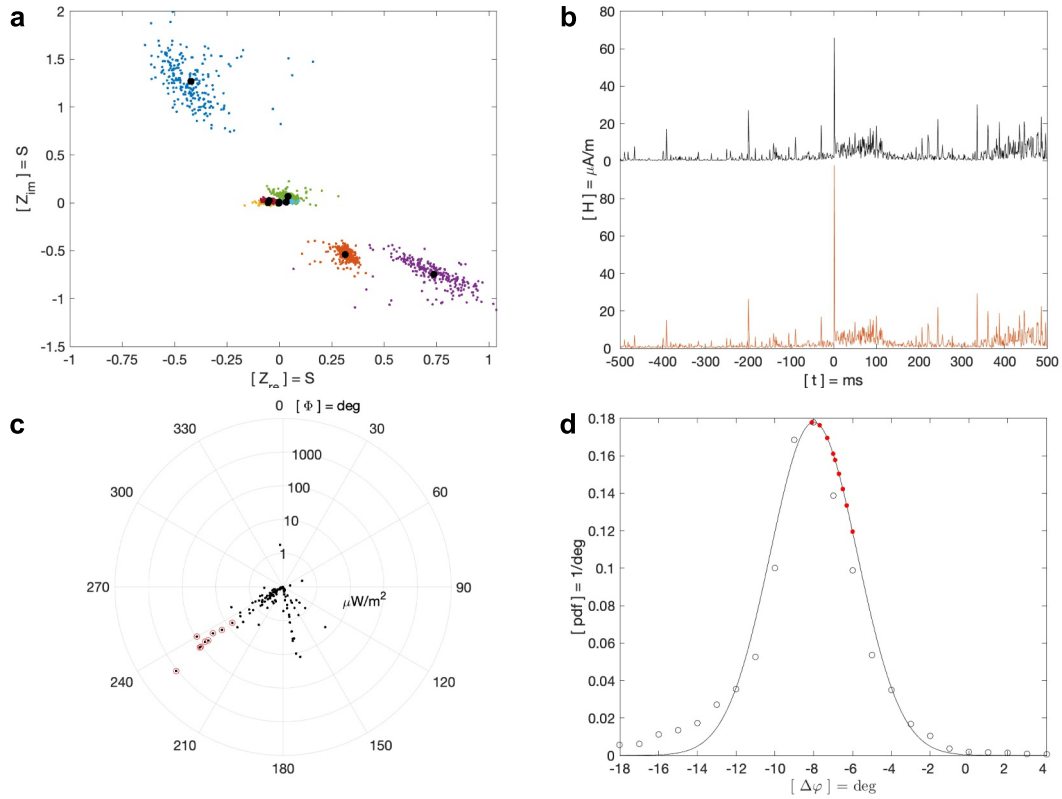

Figure 5. Coupling of electric and magnetic field measurements. (a) The nine elements of the transfer matrices at 10 kHz exhibit some scatter (colored dots) with apparent mean values (black dots). (b) The horizontal magnetic field of a sprite-producing lightning exhibits a return stroke at 0 ms followed by consecutive in-cloud strokes for ∼100 ms (black line). The horizontal magnetic field can be calculated from the measured electric fields by use of the average transfer matrix (red line). (c) The horizontal components of the cross product $\underline{S} = \underline{E} \times \underline{H}$ are used to calculate arrival azimuths of the electromagnetic waves of lightning strokes (black dots) and sprite-producing lightning strokes (red circles) with peak energy fluxes ranging from ∼10–1,000 μW/m^2. (d) The pdf of the differences between the measured arrival azimuths and those calculated from known lightning locations (circles) compares well to a normal distribution (solid line) with a mean and standard deviation of $-8.0° \pm 2.2°$). The arrival azimuth differences for sprite-producing lightning strokes are slightly smaller (red dots).

which carries the physical unit Siemens. It is expected that the mean values and scatter of the elements of the transfer matrix are frequency dependent. To illustrate this method with one example, spectra of all six electromagnetic field components are calculated every ms for 4 min (240 s) which results in complex spectral coefficients with a frequency resolution of 1 kHz to calculate transfer matrices using Equation 8. The nine complex elements of the transfer matrices are subsequently averaged over 1 s to reduce the influence from more intense lightning discharges. The coupling between the electric and magnetic fields is then described by 240 separate transfer matrices at each frequency. For example, the nine elements of the 240 transfer matrices at 10 kHz exhibit some scatter in their real and imaginary parts (Figure 5a, colored dots). The elements of the transfer matrix are therefore better defined when averaged over 240 s to reduce the scatter of the real and imaginary parts (Figure 5a, black dots). It is concluded that the measured electric and magnetic fields are well coupled with each other through the transfer matrix. This observation implies that Equation 4 can be used to calculate, or predict, magnetic fields from measured electric fields once the transfer matrix has been calculated. This hypothesis is tested for the transfer matrix at 10 kHz by calculating the horizontal magnetic field from the measured electric fields. The agreement between the predicted and measured magnetic field is excellent in this case (Figure 5b). However, the physical reasons for the scatter of the transfer matrix remain to be explored. Besides the signal to noise ratio of the source field, the transfer matrix can depend on the direction to a source due to a local anisotropy of the ground conductivity, similar to the uncertainty of direction finding discussed in Section 3.

The second method to investigate the coupling between electric and magnetic field measurements is to calculate the vector product of the electric and magnetic fields to calculate the energy flux perpendicular to the electric and magnetic fields. This method is reminiscent of the calculation of the Poynting vector in free space, that is vacuum, which is not exactly the case for electromagnetic measurements at the surface of the conducting Earth discussed here. The cross product of the electric field with the magnetic field is given by

$$\underline{S} = \underline{E} \times \underline{H} \quad \left[\mathrm{W/m^2}\right] \tag{9}$$

which can be calculated from each time step of the recordings. The two horizontal components of the vector product are used to calculate the peak energy flux and arrival azimuth of electromagnetic waves of lightning discharges (Figure 5c). The peak energy flux emanating from lightning strokes ranges between ∼0.1–1,000 $\mu W/m^2$. During the time of the recordings, nine Transient Luminous Events (TLEs) were recorded with a Watec 910Hx camera equipped with a 8.0 mm f/1.4 C-mount lens and operated at 25 frames per second. The camera recorded eight sprites and one halo during the ∼1.5 hr long recordings of the sky above a thunderstorm ∼400–430 km to the north-east of the camera. The occurrence times and locations of sprite-producing lightning strokes are identified from those positive lightning discharges reported by ENTLN that fall into the field of view of the camera and occur closest to the detection times by the video camera. The energy fluxes from the sprite-producing lightning are amongst the largest observed energy fluxes that range from ∼10–1,000 $\mu W/m^2$ (Figure 5c).

The arrival azimuths calculated from the horizontal components of the vector product between the electric and magnetic fields are 55.1° ± 2.2° when measured in the direction of the source, clockwise from geographic north. Note that the cross product points away from the source which adds 180° to the arrival azimuth. The lightning strokes with arrival azimuths pointing to the north-west and south-east are attributed to other thunderstorms (Figure 5c). It is interesting to determine the uncertainty of the arrival azimuths by calculating the difference between the observed arrival azimuth and the expected arrival azimuth calculated from the lightning locations reported by ENTLN. During the ∼1.5 hr long recordings, 6,980 lightning strokes coinciding with lightning reported by ENTLN are extracted to calculate the differences between the expected and measured arrival azimuths which are then summarized in a probability density function (pdf) (Figure 5d, black circles). This observed distribution of arrival azimuth differences compares well to a normal distribution with a mean and standard deviation −8.0° ± 2.2° (Figure 5d, black line). The mean is attributed to influences from the inhomogeneous conductivities of the ionosphere and the Earth, whereas the standard deviation is primarily attributed to the signal-to-noise ratio of the electromagnetic waves emitted by lightning strokes. The arrival azimuth differences for the TLEs exhibit a smaller mean and standard deviation −6.9° ± 0.7° (Figure 5d, red dots) which is attributed to the rotational dependence of arrival azimuth differences, probably as a result of the ionospheric conductivity tensor produced by the geomagnetic field.

In summary, the measured electric and magnetic fields are consistent with each other as quantified in detail with a transfer matrix and the vector product between electric and magnetic fields. The transfer matrix enables the calculation of magnetic fields by using the measured electric fields. The vector product enables the calculation of energy fluxes and arrival azimuths. Both methods offer results that strongly underpin the coupling between electric and magnetic fields. It is therefore concluded that measurements of horizontal electric fields at the surface of the Earth can be used for remote sensing of lightning which might offer advantages in certain applications that are discussed in the next section.

5. Summary and Conclusions

To the best of our knowledge, this contribution reports for the very first time that all six components of lightning electromagnetic fields are measured simultaneously at low frequencies from ∼100 Hz to ∼500 kHz.

The main novel contribution is a rigorous assessment of horizontal electric field measurements with emphasis on time of arrival differences which are found to be on the order of a few ns. The significance of this work lies in the use of horizontal electric fields for the quickly developing field of interferometry with arrays of low frequency radio receivers. For example, the Africa2Moon collaboration between South Africa and China aims to deploy an array of four low frequency radio receivers on the far side of the moon to survey astronomical objects at frequencies <10 MHz. This is not possible with Earth based astronomical interferometers, as a result of the

intervening ionosphere extending from ∼50–1,000 km height. With this application in mind, the deployment of interferometric arrays to measure horizontal electric fields in harsh environments can be used as a pathfinder mission with the aim to identify critical technical requirements.

The measurement of horizontal electric fields has a number of advantages. Compared to vertical electric field components, the polarisation can be used to measure approximate directions to the source (Figure 3c). Compared to magnetic field measurements with coils, the signal conditioning unit and cables are rather cost-effective which enables to scale arrays to large sizes. The length of the cables can be adjusted to meet the sensitivity requirements of particular applications. The installation of cables does not need mechanical support structures and it is therefore beneficial for efficient rapid deployments.

The first simultaneous measurement of the electromagnetic waves from sprite-producing lightning in all six electromagnetic field components is reported here. Real world experiments with horizontal dipole antennas that are aligned in parallel or aligned with cartesian coordinate systems that are rotated with respect to each other both show that the timing uncertainties of lightning strokes are a few ns. This uncertainty is attributed to the accuracy of the GNSS clocks used and it is much larger than the fundamental limit of the timing uncertainty ∼1–5 ps of the equipment and software used. The coupling between the electric and magnetic fields is exemplarily quantified by a transfer matrix and the cross product between the electric and magnetic fields. The coupling enables a calculation of (a) the expected magnetic fields from the measured electric fields, (b) the energy flux from sprite-producing lightning ∼10–1,000 $\mu W/m^2$, (c) the arrival azimuths of electromagnetic waves from lightning, and (d) the differences between the measured and expected arrival azimuths $-8.0° \pm 2.2°$. Overall, it is concluded that horizontal electric field measurements are a useful measurement with several benefits, including the ease of deployment in harsh environments, cost-effectiveness and scalability, e.g. for polarisation measurements in very large low frequency arrays.

Conflict of Interest

The authors declare no conflicts of interest relevant to this study.

Data Availability Statement

The data used for this publication are available from "Fullekrug, M., in press. Figures for publication "Six-component electromagnetic wave measurements of sprite-associated lightning." Bath: University of Bath Research Data Archive. https://doi.org/10.15125/BATH-01612".

Acknowledgments
The work of M.F. and M.K. was sponsored by the Royal Society (UK) Grant NMG/R1/180252. M.F. developed part of the technology with sponsorship from the Natural Environment Research Council (UK) under Grants NE/L012669/1 and NE/H024921/1 and the European Union's Horizon 2020 research and innovation programme under the Marie Sklodowska-Curie grant agreement 722337. L.M. was supported by the European Union's Horizon 2020 research and innovation programme under the Marie Sklodowska-Curie grant agreement 101019319. M.F. developed the concept for the experimental program, conducted the electromagnetic experiments, analysed the data and wrote the publication. M.K. provided paramount logistic support that enabled the experimental program, helped with the electromagnetic experiments, and conducted optical observations of sprites. G.D. developed the concept of the signal conditioning unit and built and calibrated the units in the laboratory. X.B. and L.M. assisted with conducting the electromagnetic experiments. All authors assisted improving the quality of the initial manuscript. M.F. wishes to thank Jeff Lapierre and Michael Stock for access to lightning data from Earth Networks, Talene Deetlefs for access to the land of Delville Country House to conduct the experiments near Carnarvon in the Karoo desert, South Africa, and Biagio Forte for the acquisition of the data acquisition unit. The lead author is particularly thankful to the thoughtful spark who planted two reserve tires into the Hillux, which were both needed during the drive on dirt roads into the Karoo desert, and the gentleman who swiftly repaired one tire in a timely manner before the third puncture happened. The authors thank two anonymous reviewers for their assistance to improve the quality of the manuscript.

References

Alcoverro, B., & LePichon, A. (2005). Design and optimization of a noise reduction system for infrasonic measurements using elements with low acoustic impedance. *Journal of the Acoustical Society of America*, *117*(4), 1717–1727. https://doi.org/10.1121/1.1804966

Bai, X., & Füllekrug, M. (2022). Coherency of lightning sferics. *Radio Science*, *57*, 1–16. https://doi.org/10.1029/2021RS007347

Bitzer, P., Christian, H., Stewart, M., Burchfield, J., Podgorny, S., Corredor, D., et al. (2013). Characterization and applications of VLF/LF source locations from lightning using the Huntsville Alabama Marx Meter Array. *Journal of Geophysical Research*, *118*(8), 3120–3138. https://doi.org/10.1002/jgrd.50271

Bor, J., Andre, K., Bozoki, T., Mlynarczyk, J., Steinbach, P., Novak, A., & Lemperger, I. (2022). Estimating the attenuation of ELF-band radio waves in the Earth's crust by Q-bursts. *IEEE Transactions on Antennas and Propagation*, *70*(8), 6973–6982. https://doi.org/10.1109/TAP.2022.3161504

Bor, J., Ludvan, B., Attila, N., & Steinbach, P. (2016). Systematic deviations in source direction estimates of Q-bursts recorded at Nagycenk, Hungary. *Journal of Geophysical Research*, *121*(10), 1–19. https://doi.org/10.1002/2015JD024712

Bor, J., Zelko, Z., Hegedüs, T., Jäger, Z., Mlynarczyk, J., Popek, M., & Betz, H. (2018). On the series of +CG lightning strokes in dancing sprite events. *Journal of Geophysical Research*, *123*, 1–18. https://doi.org/10.1029/2017JD028251

Burke, C., & Jones, D. (1992). An experimental investigation of ELF attenuation rates in the Earth-ionosphere duct. *Journal of Atmospheric and Terrestrial Physics*, *54*(3/4), 243–250. https://doi.org/10.1016/0021-9169(92)90005-6

Burke, C., & Jones, D. (1995). Global radiolocation in the lower ELF frequency band. *Journal of Geophysical Research*, *100*(D12), 26263–26271. https://doi.org/10.1029/95JD02735

Cummer, S., & Inan, U. (1997). Measurement of charge transfer in sprite-producing lightning using ELF radio atmospherics. *Geophysical Research Letters*, *24*(14), 1731–1734. https://doi.org/10.1029/97GL51791

Fraser-Smith, A. (2007). The effective antenna noise figure F_a for a vertical loop antenna and its application to extremely low frequency/very low frequency atmospheric noise. *Radio Science*, *42*, RS4026. https://doi.org/10.1029/2005RS003387

Fraser-Smith, A., McGill, P., Bernardi, A., Helliwell, R., & Ladd, M. (1991). Global measurements of low-frequency radio noise. In H. Kikuchi (Ed.), *Environmental and Space Electromagnetics* (pp. 191–200). Springer.

Füllekrug, M. (2010). Wideband digital low-frequency radio receiver. *Measurement Science and Technology*, *21*, 1–9. https://doi.org/10.1088/0957-0233/21/1/015901

Füllekrug, M., Koh, K., Liu, Z., & Mezentsev, A. (2018a). Detection of low frequency continuum radiation. *Radio Science*, *53*, 1–12. https://doi.org/10.1029/2018RS006654

Füllekrug, M., Koh, K., Liu, Z., & Mezentsev, A. (2018b). First map of coherent low frequency continuum radiation in the sky. *Radio Science*, *53*, 44–59. https://doi.org/10.1029/2018RS006705

Füllekrug, M., Liu, Z., Koh, K., Mezentsev, A., Pedeboy, S., Soula, S., et al. (2016). Mapping lightning in the sky with a mini array. *Geophysical Research Letters*, *43*, 1–7. https://doi.org/10.1002/2016GL070737

Füllekrug, M., Mareev, E., & Rycroft, M. (Eds.) (2006). *Sprites, Elves and Intense Lightning Discharges*. Springer.

Füllekrug, M., Mezentsev, A., Watson, R., Gaffet, S., Astin, I., & Evans, A. (2014). Array analysis of electromagnetic radiation from radio transmitters for submarine communication. *Geophysical Research Letters*, *41*, 1–7. https://doi.org/10.1002/2014GL062126

Füllekrug, M., Mezentsev, A., Watson, R., Gaffet, S., Astin, I., Smith, N., & Evans, A. (2015). Map of low-frequency electromagnetic noise in the sky. *Geophysical Research Letters*, *42*, 1–9. https://doi.org/10.1002/2015GL064142

Füllekrug, M., Moudry, D., Dawes, G., & Sentman, D. (2001). Mesospheric sprite current triangulation. *Journal of Geophysical Research*, *106*(17), 20189–20194. https://doi.org/10.1029/2001JD900075

Füllekrug, M., Smith, N., Mezentsev, A., Watson, R., Astin, I., Gaffet, S., et al. (2015). Multipath propagation of low-frequency radio waves inferred from high-resolution array analysis. *Radio Science*, *50*, 1–9. https://doi.org/10.1002/2015RS005781

Haspel, C., & Yair, Y. (2024). Numerical simulations of the region of possible sprite inception in the mesosphere above winter thunderstorms under wind shear. *Advances in Space Research*, *74*(11), 5548–5568. https://doi.org/10.1016/j.asr.2024.08.050

Jackson, J. (1999). *Classical electrodynamics*. Wiley.

Johnson, M., & Inan, U. (2000). Sferic clusters associated with early/fast VLF events. *Geophysical Research Letters*, *27*(9), 1–4. https://doi.org/10.1029/1999GL010757

Karunarathne, S., Marshall, T., Stolzenburg, M., Karunarathna, N., Vickers, L., Warner, T., & Orville, R. (2013). Locating initial breakdown pulses using electric field change network. *Journal of Geophysical Research*, *118*(13), 7129–7141. https://doi.org/10.1002/jgrd.50441

Lapierre, J., Sonnenfeld, R., Stock, M., Krehbiel, P., Edens, H., & Jensen, D. (2017). Expanding on the relationship between continuing current and in-cloud leader growth. *Journal of Geophysical Research*, *122*(8), 4150–4164. https://doi.org/10.1002/2016JD026189

Lyons, W. (1996). Sprite observations above the U.S. high plains in relation to their parent thunderstorm systems. *Journal of Geophysical Research*, *101*(23), 29641–29652. https://doi.org/10.1029/96JD01866

Lyu, F., Cummer, S., Lu, G., Zhou, X., & Weinert, J. (2016). Imaging lightning intra-cloud initial stepped leaders by low-frequency interferometric lightning mapping array. *Geophysical Research Letters*, *43*(10), 5516–5523. https://doi.org/10.1002/2016GL069267

Marshall, R., Inan, U., & Lyons, W. (2007). Very low frequency sferic bursts, sprites, and their association with lightning activity. *Journal of Geophysical Research*, *112*, D22105. https://doi.org/10.1029/2007JD008857

Mezentsev, A., & Füllekrug, M. (2013). Mapping the radio sky with an interferometric network of low-frequency radio receivers. *Journal of Geophysical Research*, *118*, 1–9. https://doi.org/10.1002/jgrd.50671

Nakamura, T., Sekiguchi, K., Hobara, Y., & Hayakawa, M. (2010). A comparison of different source location methods for ELF transients by using the parent lightning discharges with known positions. *Journal of Geophysical Research*, *115*, A00E39. https://doi.org/10.1029/2009JA014992

Ohkubo, A., Fukunishi, H., Takahashi, Y., & Adachi, T. (2005). VLF/ELF sferic evidence for in-cloud discharge activity producing sprites. *Geophysical Research Letters*, *32*, L04812. https://doi.org/10.1029/2004GL021943

Pasko, V. (2010). Recent advances in theory of transient luminous events. *Journal of Geophysical Research*, *115*, A00E09. https://doi.org/10.1029/2009JA014860

Pizzuti, A., Bennett, A., Soula, S., Amor, S. N., Mlynarczyk, J., Fullekrug, M., & Pedeboy, S. (2022). On the relationship between lightning superbolts and TLEs in Northern Europe. *Atmospheric Research*, *270*(106047), 1–15. https://doi.org/10.1016/j.atmosres.2022.106047

Qu, X., Xu, X., Wang, S., Li, J., Zhu, W., & Fang, G. (2018). Direction finding for radio transmitters with mini interferometric network. *Radio Science*, *53*(10), 1218–1224. https://doi.org/10.1029/2018RS006598

Reising, S., Inan, U., & Bell, T. (1999). ELF sferic energy as a proxy indicator for sprite occurrence. *Geophysical Research Letters*, *26*(7), 987–990. https://doi.org/10.1029/1999GL900123

Reising, S., Inan, U., Bell, T., & Lyons, W. (1996). Evidence for continuing currents in sprite-producing lightning flashes. *Geophysical Research Letters*, *23*(24), 3639–3642. https://doi.org/10.1029/96GL03480

Shi, D., Zheng, D., Zhang, Y., Zhang, Y., Huang, Z., Lu, W., et al. (2017). Low-frequency E-field Detection Array (LFEDA)—Construction and preliminary results. *Science China Earth Sciences*, *60*(10), 1896–1908. https://doi.org/10.1007/s11430-016-9093-9

Smith, D., Eack, K., Harlin, J., Heavner, M., Jacobson, A., Massey, R., et al. (2002). The Los Alamos Sferic Array: A research tool for lightning investigations. *Journal of Geophysical Research*, *107*(D13), 1–14. https://doi.org/10.1029/2001JD000502

Stock, M., Akita, M., Krehbiel, P., Rison, W., Edens, H., Kawasaki, Z., & Stanley, M. (2014). Continuous broadband digital interferometry of lightning using a generalized cross-correlation algorithm. *Journal of Geophysical Research*, *119*(6), 1–32. https://doi.org/10.1002/2013JD020217

Wait, J. (1990). Current flow into a three-dimensionally anisotropic conductor. *Radio Science*, *25*(5), 689–694. https://doi.org/10.1029/RS025i005p00689

Whitley, T., Füllekrug, M., Rycroft, M., Bennett, A., Wyatt, F., Elliott, D., et al. (2011). Worldwide extremely low frequency magnetic field sensor network for sprite studies. *Radio Science*, *46*, RS4007. https://doi.org/10.1029/2010RS004523

Wu, T., Wang, D., & Takagi, N. (2018). Lightning mapping with an array of fast antennas. *Geophysical Research Letters*, *45*(8), 3698–3705. https://doi.org/10.1002/2018GL077628

Yoshida, S., Wu, T., Ushio, T., Kusunoki, K., & Nakamura, Y. (2016). Initial results of LF sensor network for lightning observation and characteristics of lightning emission in LF band. *Journal of Geophysical Research*, *119*(12), 12034–12051. https://doi.org/10.1002/2014JD022065

Zhang, J., Niu, J., Xie, Z., Wang, Y., Li, X., & Zhang, Q. (2024). Simulated impacts of thundercloud charge distributions on sprite halos using a 3D quasi-electrostatic field model. *Geophysical Research Letters*, *15*(11), 1–19. https://doi.org/10.3390/atmos15111395

Zhu, Y., Stock, M., & Bitzer, P. (2021). A new approach to map lightning channels based on low-frequency interferometry. *Atmospheric Research*, *247*(105139), 1–10. https://doi.org/10.1016/j.atmosres.2020.105139